Deciphering the Effect of Fe and Cu in Pd Lattice for Oxygen Reduction Reaction

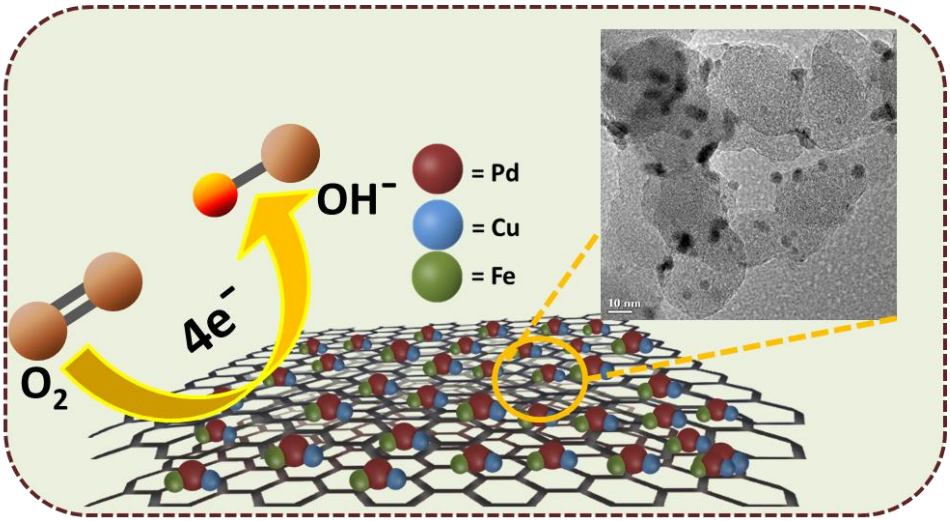

In this Chapter, we have studied the synthesis of a hybrid PdFeCu electrocatalyst on Vulcan carbon support. The incorporation of Cu and Fe in Pd lattice modifies the electronic environment and eventually enhances the ORR performance than the Pd/C. The PdFeCu NPs uniformly embedded on the carbon support and results in a strong metal support interaction (SMSI). This SMSI hinders agglomeration of the PdFeCu NPs, providing more active sites and improving the intrinsic activity of the PdFeCu/C electrocatalysts. As a result, it demonstrates several promising characteristics than the other reported counterparts and comparable to Pt/C. CA and ADT results demonstrate that PdFeCu/C exhibits excellent durability and stability in 0.1M KOH solution. Furthermore, PdFeCu/C exhibit excellent MeOH tolerance which is higher than the commercial Pt/C. These analyses suggest that PdFeCu/C could be a promising candidate for ORR and direct methanol fuel cells (DMFCs), offering a viable alternative to Pt-based electrocatalysts. The experimental procedures for the synthesis, characterization techniques, and electrocatalytic measurements were described in Chapter 2.

5.1. Introduction

PEMFCs are regarded as advantageous energy converters since they generate energy without emitting any harmful gases. The cathodic ORR is crucial in PEMFCs. However, the reaction has sluggish kinetics and irreversible mechanisms [1-7]. The catalyst's performance is the only factor that determines ORR efficiency. The most efficient electrocatalysts for ORR are known to be Pt-based catalysts [1-4]. However, their commercial application has been limited due to their extremely high cost, scarcity, lack of stability, and CO poisoning. Pd is a promising alternative to Pt for ORR due to its identical crystallographic and electronic structures [5-9]. The abundance of Pd is more than Pt with a mass abundance of 0.015 ppm compared to 0.005 ppm of Pt and less expensive [5-9]. On the other hand, strong oxygen-containing intermediate adsorption during ORR can significantly suppress the active sites, turning it into the rate-limiting step at high potentials. It is, therefore, extremely desirable to achieve high activity to achieve a moderate oxygen binding energy on the catalyst surface [12–13]. Pd has stronger adsorption strength for oxygen-intermediate species than Pt, which reduces catalytic activity towards ORR. It has been found that the binding strength of adsorbed oxygen species can be substantially reduced by adjusting the strain and ligand influence on the catalyst [9-15]. To induce these effects an effective strategy is incorporating early transitional metal, for instance, Cu, Fe, Ni, or Co into the Pd lattice [10-28]. Due to the addition of transitional metals and the ensuing charge transfer, the modified electronic structure produces the ligand effect. On the other hand, the strain effect arises from the induced lattice mismatch. The resulting strain and ligand effect causes a downward shift of the *d*-band center, reducing the binding strength of adsorbed intermediates and significantly enhancing ORR activity [12-15]. Incorporating other metals into Pd NPs improve the performance and lowers the consumption of high-cost Pd. Thus, it is desirable to integrate inexpensive metals to enhance the catalytic activity of Pd NPs further and reduce the cost of nanocatalyst [21–27]. Motivated by all the discussed advantages, we added Cu and Fe into the Pd lattice to reduce the Pd content while maintaining its catalytic activity towards ORR.

5.2. Results and Discussion

5.2.1. Characterization of the PdFeCu/C, PdFe/C and *PdCu/C*

The crystallographic structures of PdFeCu/C, PdFe/C, PdCu/C, and Pd/C were obtained by powder XRD analysis and are shown in Figure 5.1a. It is observed that each samples have a peak near 26°, which corresponds to the (002) plane of Vulcan XC-72R carbon. The peaks observed at 39.9°, 46.4°, and 67.8° in Pd/C, which are consistent with the (111), (200), and (220) crystalline facets of *fcc* Pd (JCPDS 87-0641). These peaks are also observed in each sample with slight shifting to higher 2θ degree, indicating the lattice contraction due to the incorporation of Cu or Fe into the Pd lattice. Therefore, compared to Pd/C (0.392 nm), a smaller lattice parameter is seen for PdFeCu/C (0.389 nm), PdFe/C (0.391 nm), and PdCu/C (0.390 nm). The additional peak observed at 29.8° 35.2° 56.7° and 62.4° in PdFe/C is due to the formation of Fe_3O_4 corresponding to JCPDS 65-1346. These peaks were also observed in PdFeCu/C with slight shifting to PdFe/C system. The loading of the metal obtained by TGA analysis is ~20% in PdFeCu/C, PdFe/C and PdCu/C and presented in Figure 5.1b. It shows a speedy weight loss of the hybrid NPs at about ~380 °C due to the oxidation of carbon to carbon dioxide in the adequate air environment. The residue obtained after the burning of all the carbon compounds gives information about the loading of the total metal content on the carbon support.

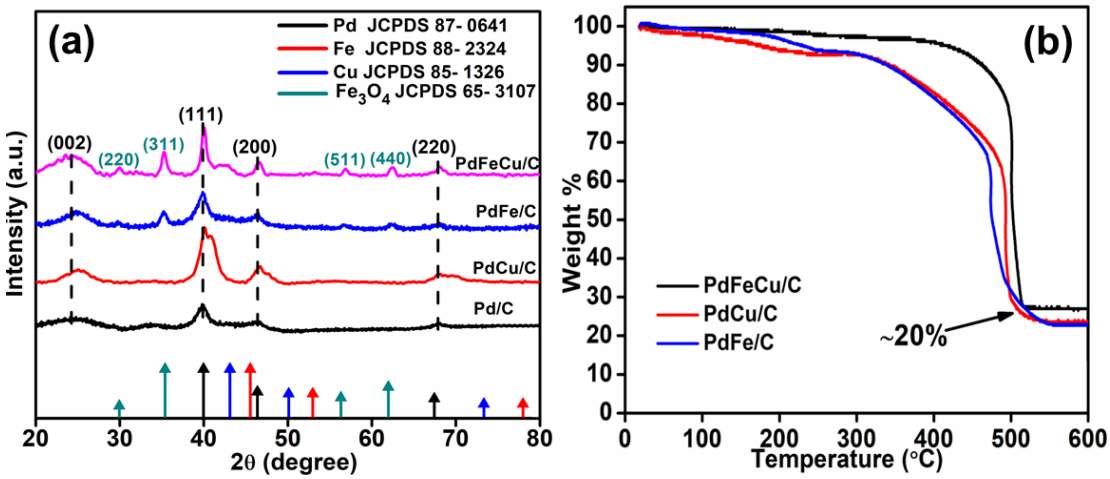

Figure 5.1: (a) XRD patterns of PdFeCu/C, PdFe/C, PdCu/C and Pd/C, (b) TGA profiles of PdFeCu/C, PdFe/C, and PdCu/C in air atmosphere.

The presence of all four elements (Pd, Fe, Cu and C) in the NPs was confirmed by the energy-dispersive X-ray spectroscopy analysis, which reveals the homogeneous distribution of Pd, Fe, Cu and C as inferred from the elemental mappings (Figure 5.2). The EDX patterns and elemental maps of PdFeCu/C which proved the existence of only detectable elements in the sample. The atomic percentage or the composition ratios of the elements in the PdFeCu/C were consistent with the metal ratio taken during the synthesis, i.e., 1:1:1. The metal loading on the carbon substrate from EDX analysis corroborated well with the TGA results.

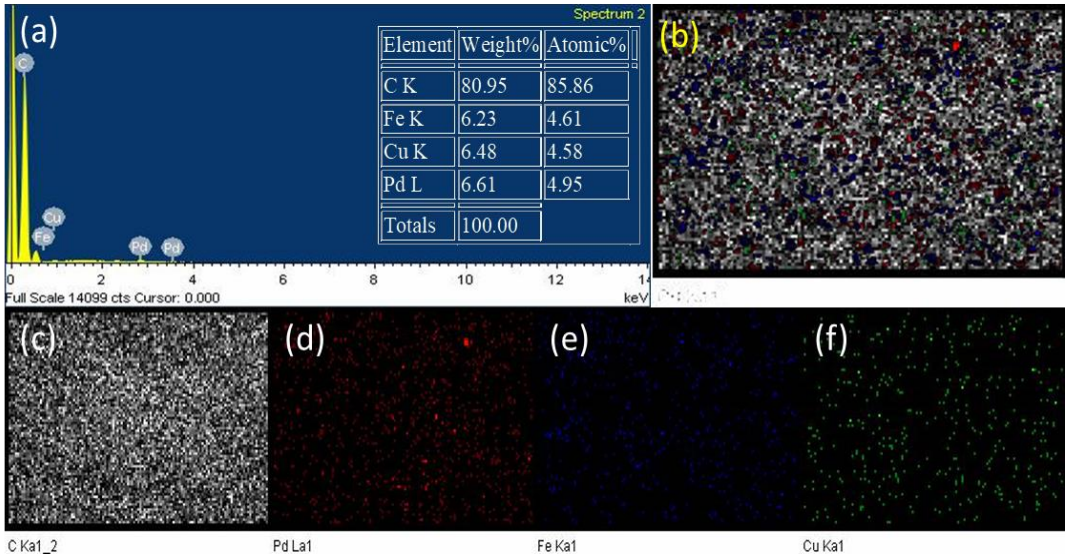

Figure 5.2: (a) EDX spectrum of PdFeCu/C hybrid (inset: shows the table for elemental composition), (b) the overlayer elements maps of C, Pd, Fe and Cu, and (c)-(f) elemental maps for individual C, Pd, Fe and Cu, respectively.

TEM images of PdFeCu/C presented in Figure 5.3 to gain information on morphology and structure details. The TEM images confirmed that the PdFeCu NPs were uniformly embedded on the carbon surface. The particle size distribution was in the range of 1–8 nm, and the average size was 4 nm (Figure 5.3a, inset particle size distribution). A significant number of PdFeCu active sites are expected to be available owing to the small particle size and homogenous particle size distribution (Figure 5.3b). In contrast, the carbon surface imparts an effective electron pathway. Additionally, some discontinuation in lattice fringes in HRTEM images observed which indicates the presence of defects in the sample (the red arrow region shown in Figure 5.3c). The defects in materials can enhance electrocatalytic activity by providing active sites, facilitating mass transport,

modifying the electronic structure, increasing surface area, and promoting synergistic effects with the catalytic material [28, 29]. These effects can collectively improve the catalytic performance of the hybrid NPs.

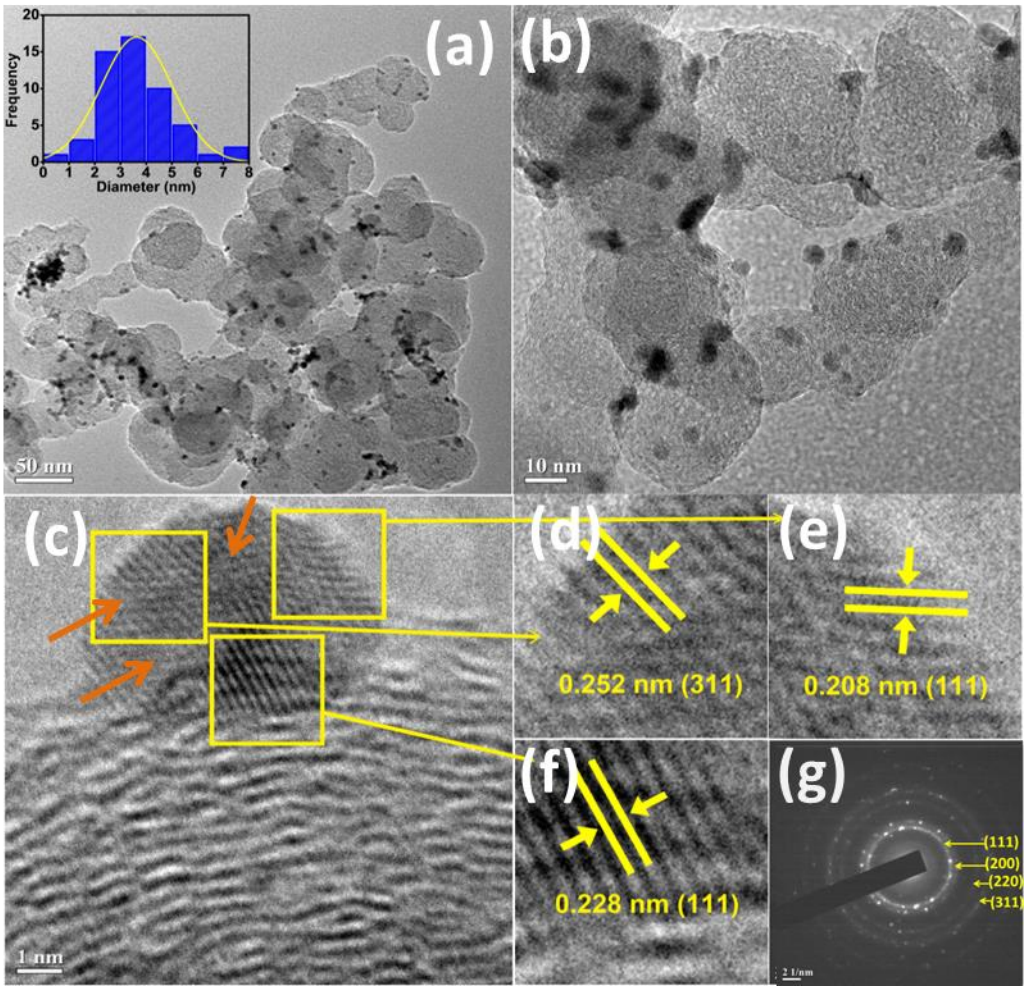

Figure 5.3: (a) Low-magnification (inset: Particle size distribution histogram) and (b) high-magnification TEM images of PdFeCu/C, (c) high-resolution TEM (HRTEM) image of PdFeCu/C, (d-f) the magnified HRTEM image enlarged from region marked by squares in (c), (g) SAED pattern.

The HRTEM image displays a lattice fringes pattern with d-spacing of 0.228 nm, 0.208 nm and 0.252 nm, corresponding to the (111) plane of Pd, (111) plane of Cu and (311) plane of Fe_3O_4, respectively (Figure 5.3d, e, f). The SAED pattern suggests the polycrystalline nature of PdFeCu/C, as shown in Figure 5.3g. These rings can be indexed to the (111), (200), (220) and (311) *fcc* lattice planes of Pd, similar to the XRD findings. Based on the above TEM results, we can say that uniformly dispersed Pd-based NPs on the carbon surface can be effectively synthesized by a simple solvothermal method.

XPS was used to analyse the surface characteristics and chemical states of PdFeCu/C and presented in Figure 5.4. The survey XPS spectra analysis of the PdFeCu/C sample revealed the presence of Pd, Fe, Cu, and C (Figure 5.4a). The high resolution Pd 3d spectra were deconvoluted into two peaks corresponding to $3d_{5/2}$ (336.3eV) and $3d_{3/2}$ (341.6 eV) shown in Figure 5.4b [28, 30, 31]. The peaks at 336.3 and 341.6 eV are assigned to the binding energies of Pd (0) and those at 337.6 and 343.1 eV are attributed to Pd (II) [28,30,31], respectively and the peak fitting data are presented in Table 5.1. In the deconvoluted spectrum of high-resolution Fe 2p (Figure 5.4c), the peaks at 710.8 and 723.7 eV are assignable to Fe (II), while the peaks at 713.1 and 725.7 eV are indicative of Fe (III) [32-35]. The peak observed at 705.0 eV, significantly smaller in comparison to bivalent and trivalent iron peaks, suggests the presence of Fe (0). Moreover, two shake-up satellite peaks are evident on the higher energy sides of the primary peaks (at 719.6 and 730.0 eV), attributed to surface-oxidized Fe(II)/Fe(III) [33-36]. The deconvoluted XPS spectrum of Cu 2p (Figure 5.4d) reveals the presence of Cu(0) and Cu(II) in the synthesized PdFeCu/C. Peaks at 932.4 and 952.3 eV are attributed to Cu(0), while peaks at 934.7 and 954.6 eV signify Cu(II). The three satellite peaks that appear at 941.3, 944.1, and 962.8 eV are due to the excitation of surplus electrons to higher energy states [31-32, 35, 36]. The C 1s peak exhibits three distinct components (C−C, C−O, and O=C−O) centered at 284.6, 286.0, and 287.5 eV, respectively [28]. The pronounced intensity of the C−C bond signifies the presence of sp^3 carbon within the reported NPs (Figure 5.4e). Additionally, the XPS spectra of PdFe/C and PdCu/C (Figure 5.5 and 5.6) depicts the presence of C, Pd, and Fe in PdFe/C, and C, Pd, and Cu in PdCu/C, respectively.

The Pd 3d spectra of PdFeCu/C, PdFe/C PdCu/C and Pd/C in Figure 5.4f show the positive shift of 0.18 eV to higher binding energy compared to that of Pd/C probably owing to electron transfer among Pd, Fe and Cu. The BEs related to Pd $3d_{5/2,3/2}$ PdFeCu/C, PdFe/C PdCu/C and Pd/C are listed in Table 5.2. The change in binding energy suggests that the *d*-band center of Pd may shift downward, which is conducive to weaken the interaction between the Pd surface and adsorbates, thereby enhancing the catalytic activity [28, 30, 31]. It is proven that the reduced Pd *d*-band center decreases the adsorption of intermediates on its surface, activating the metallic NPs in an electrode reaction-promoting manner. Additionally, it has been observed that the lattice contraction (which can be observed by XRD study) appeared after Pd was incorporated with other

metals, which lowered its *d*-band center [28, 30, 31]. All these components improve ORR properties.

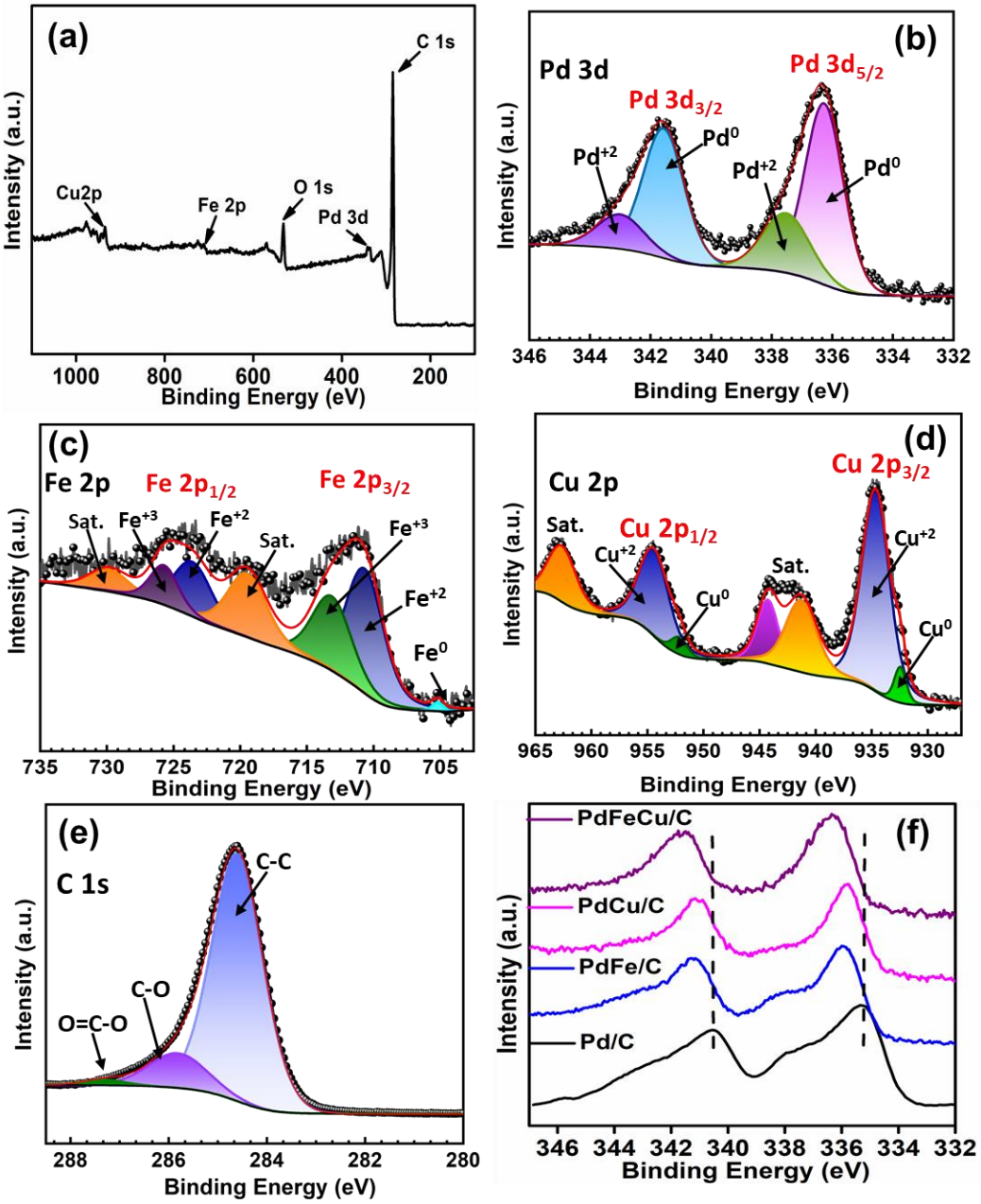

Figure 5.4: (a) XPS survey spectrum of PdFeCu/C, high resolution XPS spectra of (b) Pd 3d, (c) Fe 2p, (d) Cu 2p, and (e) C 1s of PdFeCu/C, (f) correlation of binding energy change of Pd 3d of PdFeCu/C, PdFe/C, PdCu/C and Pd/C.

Table 5.1: Binding energy values corresponding to various from high resolution XPS spectrum of PdFeCu/C.

Element	Peak assignment		Binding Energy (eV)
C	C-C		284.6
	C-O		286.0
	O=C-O		287.5
Pd	Pd 3d $_{3/2}$	Pd(0)	341.6
		Pd(II)	343.1
	Pd 3d $_{5/2}$	Pd(0)	336.3
		Pd(II)	337.6
Fe	Fe 2p $_{1/2}$	Fe(II)	723.7
		Fe(III)	725.7
	Fe 2p $_{3/2}$	Fe(II)	710.8
		Fe(III)	713.1
		Fe(0)	705.0
Cu	Cu 2p $_{1/2}$	Cu(0)	952.3
		Cu(II)	954.6
	Cu 2p $_{3/2}$	Cu(0)	932.4
		Cu(II)	934.7

Table 5.2: Comparison of BE related to Pd $3d_{5/2, 3/2}$ from XPS analysis

Electrocatalysts	**Pd $3d_{5/2}$ (eV)**	**Pd $3d_{3/2}$ (eV)**
PdFeCu/C	336.3	341.6
PdFe/C	336.1	341.2
PdCu/C	336.1	341.4
Pd/C	335.2	340.4

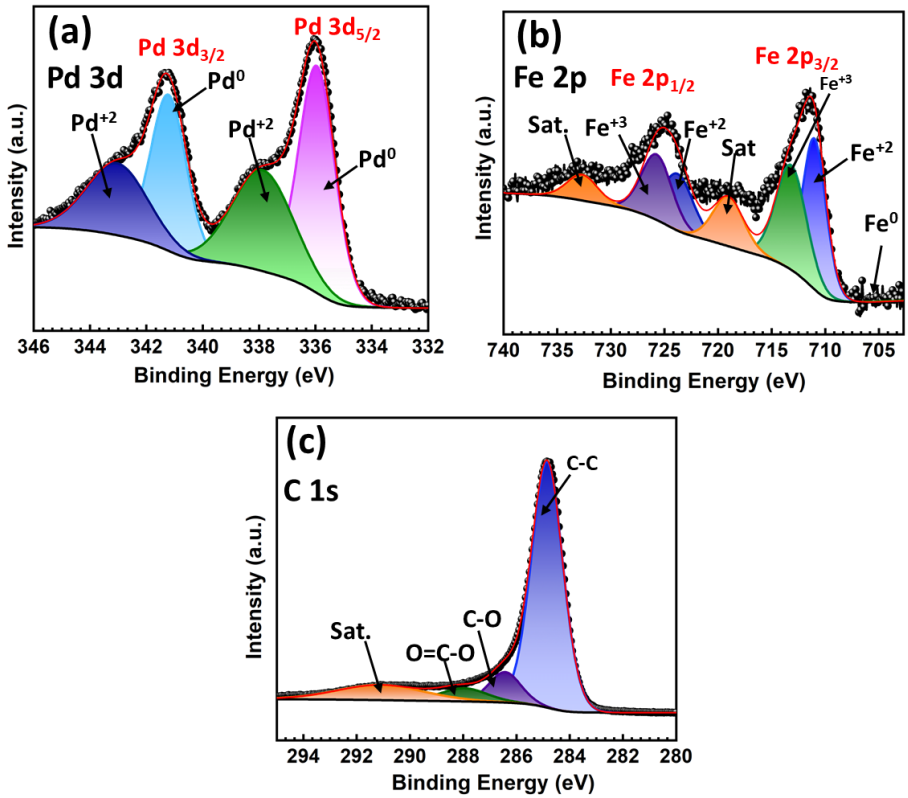

Figure 5.5: High resolution XPS spectra of (a) Pd 3d, (b) Fe 2p, and (c) C 1s of PdFe/C.

Furthermore, the XPS spectra of PdFe/C and PdCu/C presented in Figure 5.5 and 5.6 depicts the presence of C, Pd, and Fe in PdFe/C, and C, Pd, and Cu in PdCu/C, respectively. Upon deconvolution and fitting, all peaks were found to possess nearly identical binding energies to PdFeCu/C, indicating successful synthesis of PdFe/C and PdCu/C. The binding energies of PdFeCu/C slightly changes which indicates that incorporation of Cu and Fe changes the electronic environment of Pd and eventually results in changes in BE values. Notably, in PdCu/C, the intensity of the metallic Cu peak notably increases compared to PdFeCu/C, suggesting a higher proportion of metallic Cu in PdCu/C.

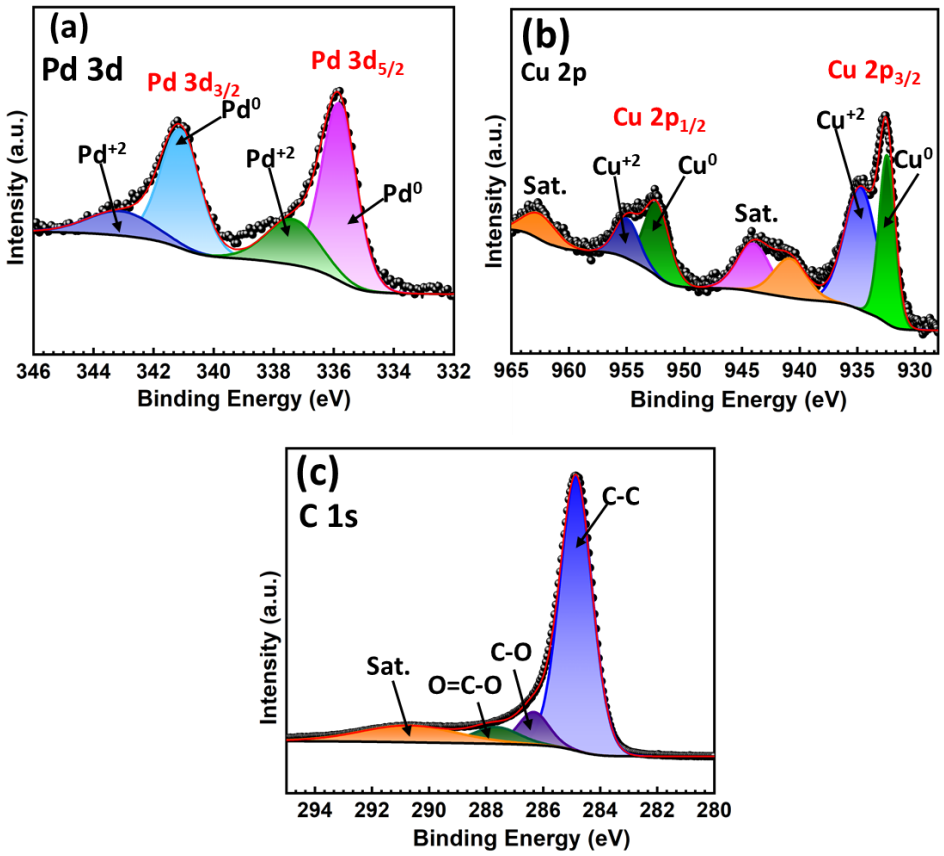

Figure 5.6: High resolution XPS spectra of (a) Pd 3d (b) Cu 2p and (c) C 1s of PdCu/C.

5.2.2. Electrocatalytic Activity towards ORR

Analogous to previous chapters, CV and LSV analysis were done to measure the ORR performance of the of PdFeCu/C, PdFe/C, PdCu/C, Pt/C and Pd/C electrocatalysts. The CV curves in N_2- and O_2-saturated 0.1M KOH solution were recorded in the potential range from 0.2 to 1.2 V *vs.* RHE at a scan rate of 50 mVs^{-1} (Figure 5.7a). The current in the reduction peak increases in an O_2-saturated atmosphere, implying that the electrocatalysts undergo electrochemical reduction in 0.1M KOH solution. The ORR kinetics in an O_2-saturated 0.1M KOH solution were determined using RDE measurements at different rotation rates from 400 to 3600 rpm, as shown in Figure 5.7b. As the rotation increases from 400 to 3600 rpm, the current density also increases due to increase in the mass transfer rate.

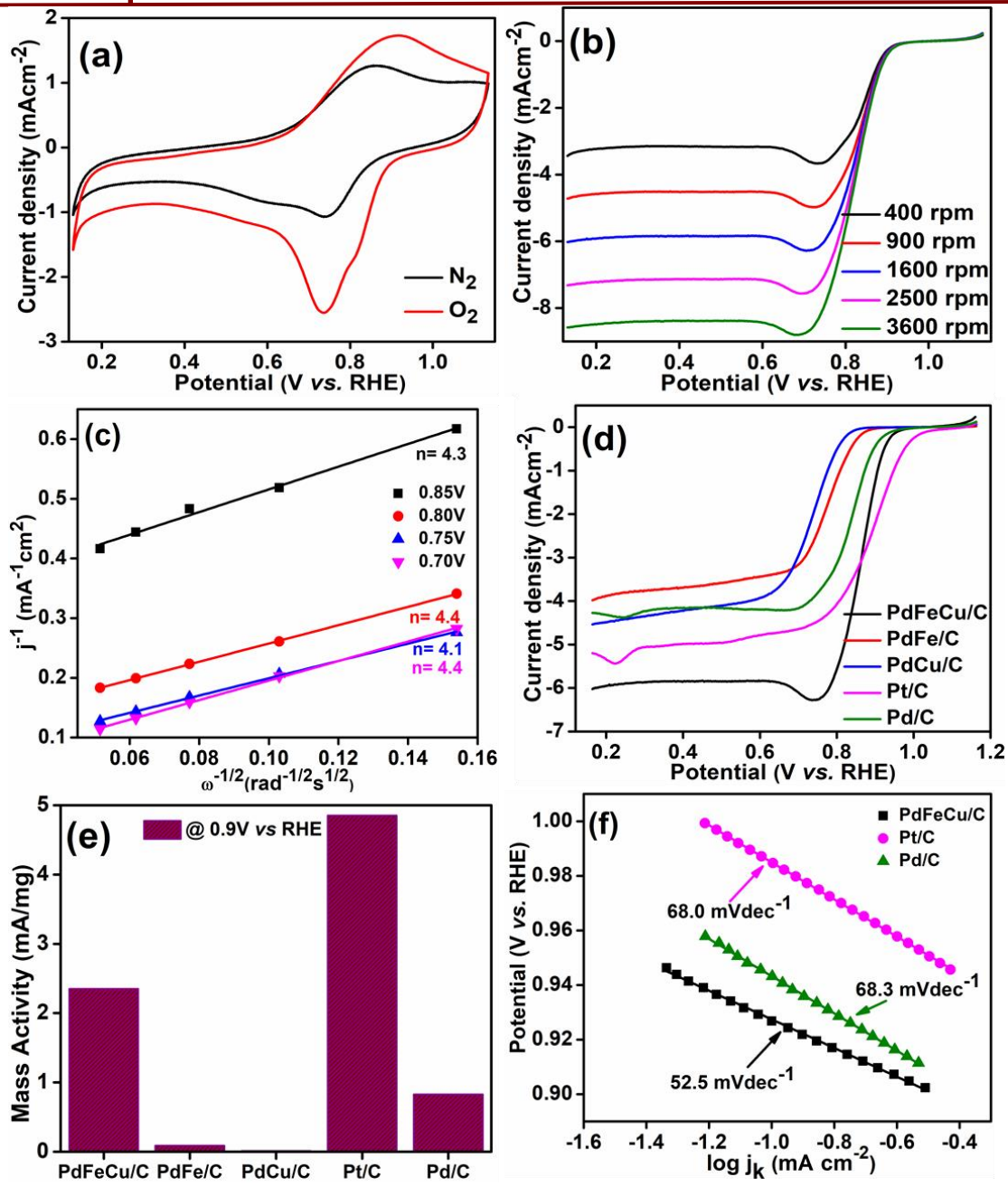

Figure 5.7: ORR electrocatalytic activity of electrocatalysts: (a) CV curves of PdFeCu/C in N_2- and O_2-saturated 0.1 M KOH electrolyte (scan rate = 50 mVs^{-1}), (b) LSV plots of PdFeCu/C at a scan rate of 10 mVs^{-1} in O_2-saturated 0.1 M KOH solution, (c) corresponding K−L plots at various potentials (inset: plot of n *vs.* potential), (d) comparison of LSV curves of PdFeCu/C, Pt/C, Pd/C, PdFe/C and PdCu/C at 1600 rpm in O_2-saturated 0.1 M KOH solution, (e) mass specific activities of PdFeCu/C, PdFe/C, PdCu/C, Pt/C and Pd/C at 0.9V and (f) Tafel plots of PdFeCu/C, Pt/C and Pd/C.

The number of electrons transferred (n) in the ORR process can be determined from the K-L plots in Figure 5.7c using these ORR polarisation curves. The derived plots exhibit a good linear relationship, suggesting the first-order reaction kinetics toward the concentration of dissolved oxygen during the ORR process. Furthermore, the n for PdFeCu/C were calculated to be close to four (Figure 5.7c) at different potentials, indicating the mechanism of this catalytic process is $4e^-$, the pathway of producing OH^-. Due to the low overpotential involved, the $4e^-$ pathway is often preferred over the $2e^-$ pathway. The polarisation curves in O_2-saturated 0.1M KOH solutions at 1600 rpm are compared with PdFeCu/C, PdFe/C, PdCu/C, Pt/C and Pd/C to understand which electrocatalysts are superior for the ORR process (Figure 5.7d). It was observed that PdFeCu/C also had an early onset potential (E_{onset} = 0.97V), half wave potential ($E_{1/2}$ = 0.87V) and higher limiting current density (j_m= -6.00 mA cm^{-2}) than the other catalysts and comparable with Pt/C (E_{onset}= 1.00, $E_{1/2}$ = 0.89V, j_m= -5.19 mA cm^{-2}) under identical conditions. A higher positive starting potential indicates that the reduction reaction begins at the earliest possible time. A comparison of ORR parameters of synthesized electrocatalysts with state-of-the-art Pt/C and Pd/C are compared (Table 5.3) and it is observed that PdFeCu/C displays superior ORR parameters than the other counterparts. The enhanced ORR activity of PdFeCu/C can be ascribed to the synergistic effect among Pd, Fe and Cu in the NPs and their proper embedment by a thin layer of the carbon support, promoting the superior ORR activity. The mass specific activities (MA) of all catalysts were obtained by normalizing kinetic current to the mass loading of the metal on the electrode. The MA of PdFeCu/C at different potentials in the kinetic region was the highest among all the electrocatalysts and comparable to Pt/C (Figure 5.7e). This value indicates that PdFeCu/C exhibits excellent catalytic activity toward ORR compared to the other synthesized samples for an identical amount of mass loading. The Tafel slope is a useful parameter to determine the kinetics of the ORR process, which can be fitted from the polarization curves of the catalysts [28, 36, 37]. Figure 5.7f shows the PdFeCu/C has smaller Tafel slope (52.5 $mVdec^{-1}$) than the commercial Pt/C (68.0 $mVdec^{-1}$) and commercial Pd/C (68.3 $mVdec^{-1}$). The low Tafel slope value suggests faster kinetics and a high rate of electron transfer from PdFeCu/C towards ORR. These results reveal that the intrinsic activities of PdFeCu/C are the best among these catalysts. The CV, LSV curves of PdFe/C and PdCu/C along with their corresponding KL plots are also presented in Figures 5.8.

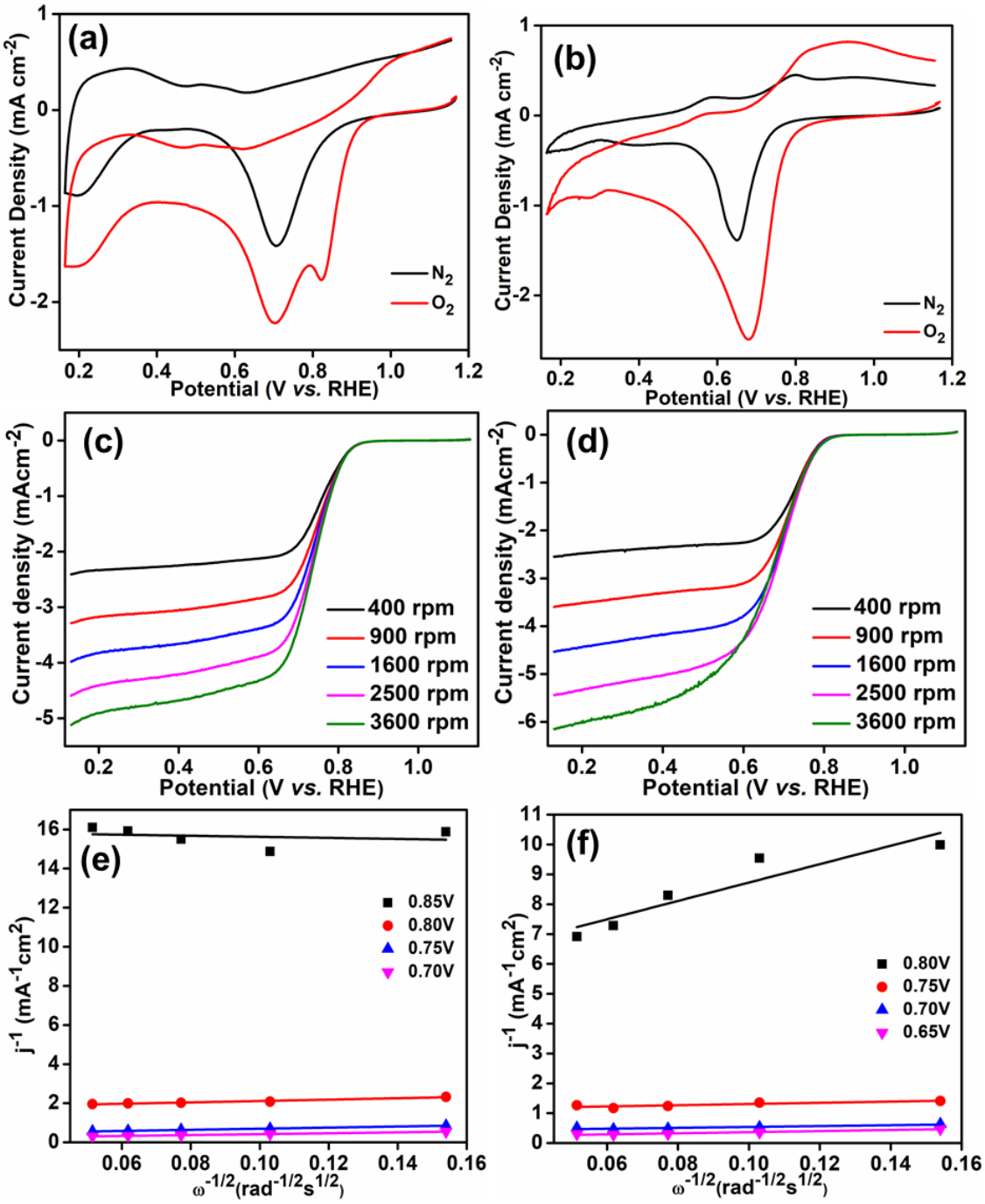

Figure 5.8: (a,b) CV plots of PdFe/C and PdCu/C, N_2- and O_2-saturated 0.1 M KOH solution with a scan rate of 50 mVs^{-1}, (c,d) rotating rate-dependent ORR polarization curves for respective electrocatalysts with the scan rate of 10 mVs^{-1}, and (e,f) corresponding KL plots of PdFe/C and PdCu/C at different potentials.

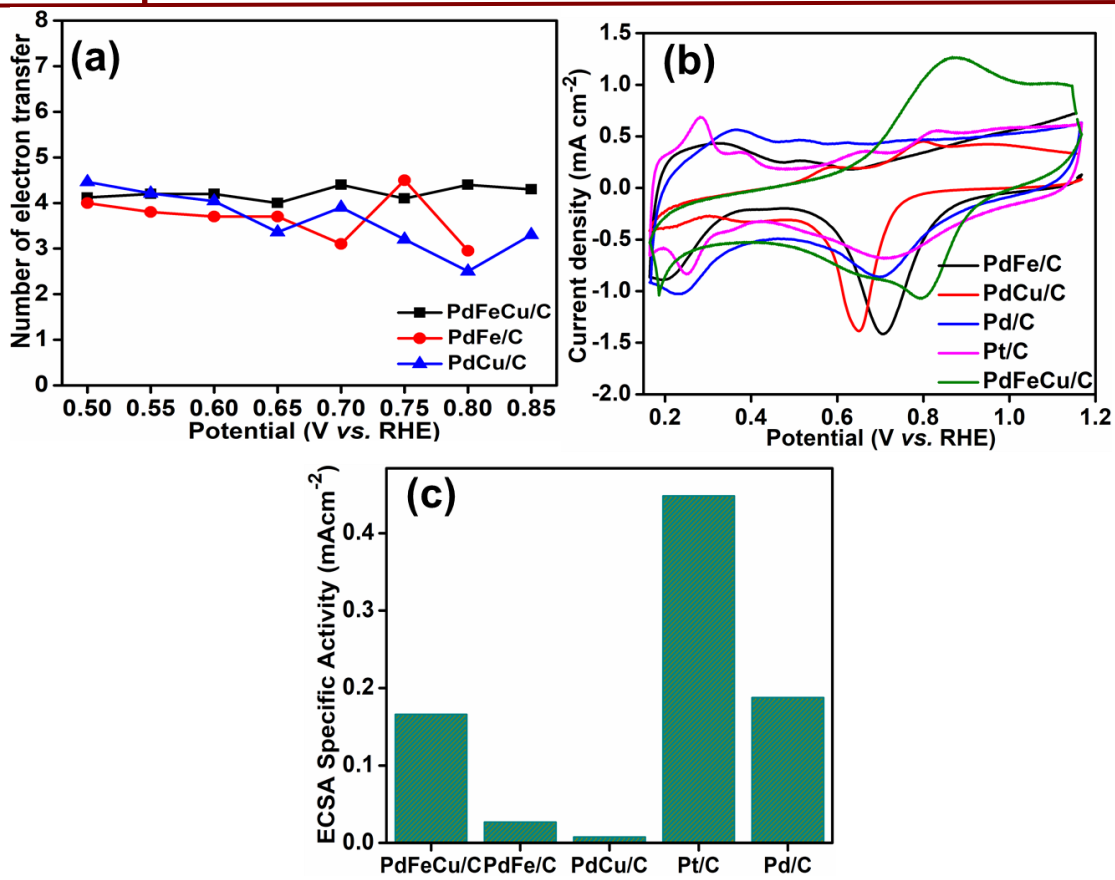

Figure 5.9: (a) Number of electrons transferred over a wide potential range PdFeCu/C, PdFe/C, PdCu/C, (b) CV curves of PdFeCu/C, PdFe/C, PdCu/C, Pt/C and Pd/C in N_2-saturated 0.1 M KOH solution with a scan rate of 50 mVs^{-1}, and (c) ECSA specific activities of PdFeCu/C, PdFe/C, PdCu/C, Pt/C and Pd/C at 0.85 V *vs.* RHE.

Furthermore, the 'n' value for PdFeCu/C, PdFe/C and PdCu/C at wide potential range were calculated and it found to be close to four for PdFeCu/C. Figures 5.9a indicating the mechanism of this catalytic process is $4e^-$, the direct pathway of producing OH^- from ORR. Due to the low overpotential involved, the $4e^-$ pathway is often preferred over the $2e^-$ pathway. The Electrochemically active surface area (ECSA) is an important parameter to evaluate the catalytic performance of electrocatalysts. It is calculated from CV curves in an N_2-saturated atmosphere in the 0.1 M KOH solution and the CV curves of all the samples are presented in Figure 5.9b. The ECSA values of as-prepared materials can be calculated by the following formula ECSA = Q/SL, [9,28] where L is the loading of Pd, Q is the charge estimated from PdO stripping, and S is a constant equal to 424 μCcm^{-2} considering that the surface is covered with a PdO monolayer. The PdFeCu/C electrocatalysts show the highest ECSA and follows the following sequence PdFeCu/C (91.9 m^2g^{-1}) > PdCu/C (72.8 m^2g^{-1}) > Pt/C (29.5 m^2g^{-1}) > Pd/C (21.7 m^2g^{-1}) > PdFe/C

(17.8 m^2g^{-1}). It may be associated with the high ECSA value of PdFeCu/C with their uniform embedment on the carbon surface, which will provide abundant active sites on the inside and outside. The ECSA specific activities (ECSA SA) at 0.85 V *vs.* RHE were obtained by normalizing the kinetic current with the ECSA and presented in Figure 5.9c. Especially, PdFeCu/C achieves the highest ECSA SA (0.165 mA cm^{-2}) at 0.85 V, which are 6.2 and 22.3 times higher than those of PdFe/C and PdCu/C electrocatalyst. The excellent ORR activity is mainly because the introduction of Fe and Cu can induce reduced oxygen adsorption energy due to the downshift of the *d*-band center of Pd [9, 28, 37].

Table 5.3: Summary of onset potential (E_{onset}), half wave potential ($E_{1/2}$), current density (j_m) and electrochemically active surface area (ECSA) of PdFeCu/C, PdCu/C, PdFe/C Pt/C and Pd/C toward ORR at 1600 rpm.

Sl No.	**Electrocatalysts**	**E_{onset} (V *vs.* RHE)**	**$E_{1/2}$ (V *vs.* RHE)**	**j_m (mA cm^{-2})**	**ECSA (m^2g^{-1})**
1	PdFeCu/C	0.97	0.87	-6.00	91.9
2	PdCu/C	0.88	0.74	-4.51	72.8
3	PdFe/C	0.86	0.78	-3.95	17.8
4	Pt/C	1.00	0.89	-5.19	29.5
5	Pd/C	0.94	0.83	-4.26	21.7

In addition to the catalytic activity, the long-term stability and durability of the electrocatalyst is another crucial factor for their practical implementation in FCs. The long-term stability of PdFeCu/C and commercial Pt/C is evaluated by performing the CA analysis at 0.53V *vs.* RHE for 6h (Figure 5.10a). After 6h reaction time, the PdFeCu/C retains 96.6% of the initial activity, while Pt/C only retains 72.5%. The integrity of the carbon support directly affects the stability of the active sites since they are dispersed throughout the former as evident from the TEM images. Carbon corrosion is one of the factors that might cause performance degradation since it can degrade or reduce active centers [38]. An accelerated ADT was carried out to examine the structural integrity of the electrocatalysts. It was determined by doing an LSV analysis before and after the

repeated 10000 CV cycles under O_2-saturated environment. This experimental condition is similar to an activated corrosive environment and examining the changes that occurred on $E_{1/2}$ owing to ADT reveals significant insight into the durability of the electrocatalyst. The LSV curve of PdFeCu/C nearly matches the initial LSV curve (Figure 5.10b), indicating the outstanding stability of PdFeCu/C. As shown in Figure 5.10c, the PdFeCu/C displays excellent stability with only 5 mV degradation in $E_{1/2}$, whereas for PdFe/C and PdCu/C were 110 mV and 56 mV, respectively.

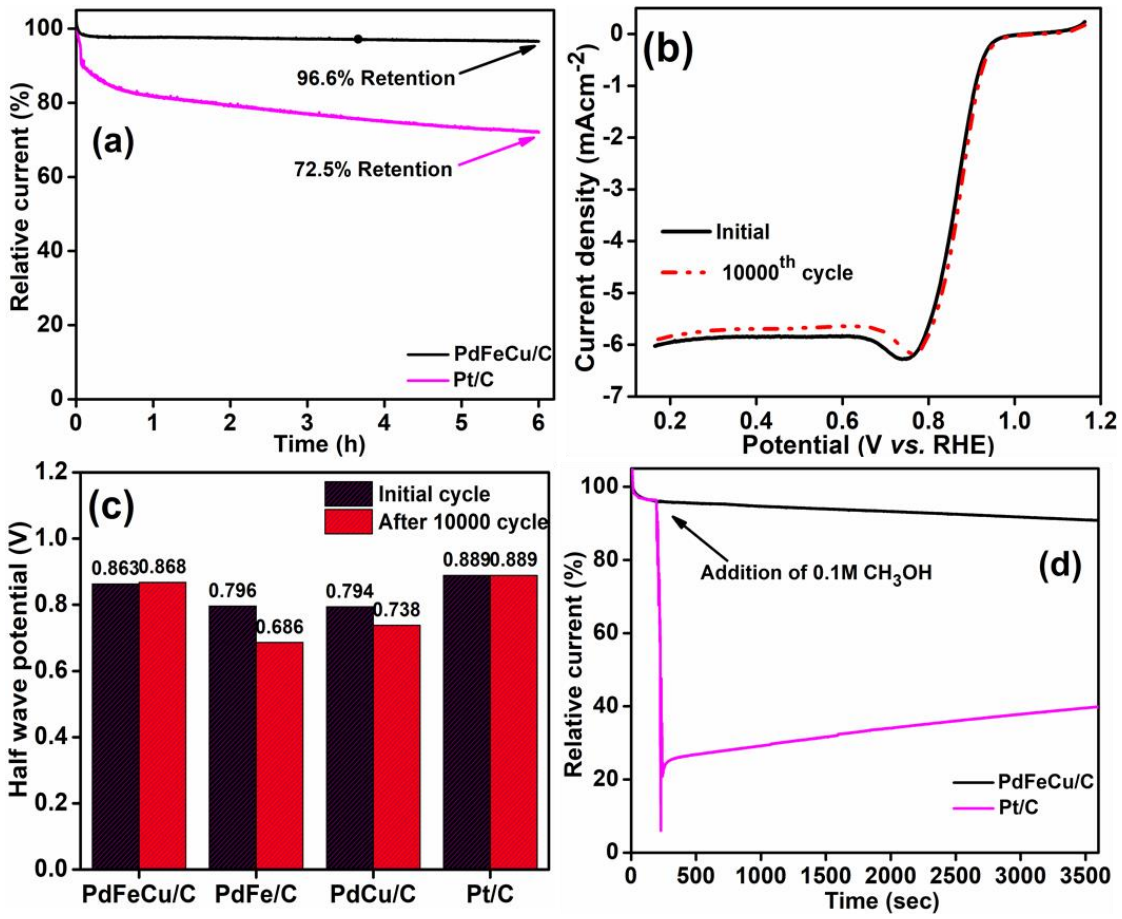

Figure 5.10: Stability and durability test of electrocatalysts: (a) CA plots of PdFeCu/C and Pt/C measured in an O_2-saturated 0.1 M KOH electrolyte at a rotation of 1600 rpm, (b) ORR polarization LSV plots of PdFeCu/C at 1600 rpm before and after 10000 cycles. (c) half-wave potentials before and after the ADT of all the electrocatalysts, and (d) CA curves of a methanol tolerance test of PdFeCu/C and Pt/C for 3600s.

Methanol crossover from the anode to the cathode could be considered one of the main factors leading to the performance loss in DMFCs. An ideal electrocatalyst for the cathode in DMFCs ought to exhibit superior activity toward oxygen reduction and high methanol resistance. To evaluate the tolerance of PdFeCu/C and Pt/C to methanol poisoning, 0.1 M CH_3OH was added to the electrolyte during the CA measurements. As seen in Figure 5.10d, while the Pt/C experiences a sudden drop in current after the addition of methanol, the observed current loss for PdFeCu/C is negligible, suggesting that the prepared nanomaterial has great methanol tolerance. The outstanding methanol tolerance capability of PdFeCu/C introduces its possible application as a non-Pt electrocatalyst for DMFC in alkaline medium. After the 10000 durability test the MA and ECSA SA for both PdFeCu/C and Pt/C are compared in Figure 5.11, the change in MA (Figure 5.11a) and ECSA SA (Figure 5.11b) of PdFeCu/C is comparable to commercial Pt/C, indicating that PdFeCu/C has commendable activity.

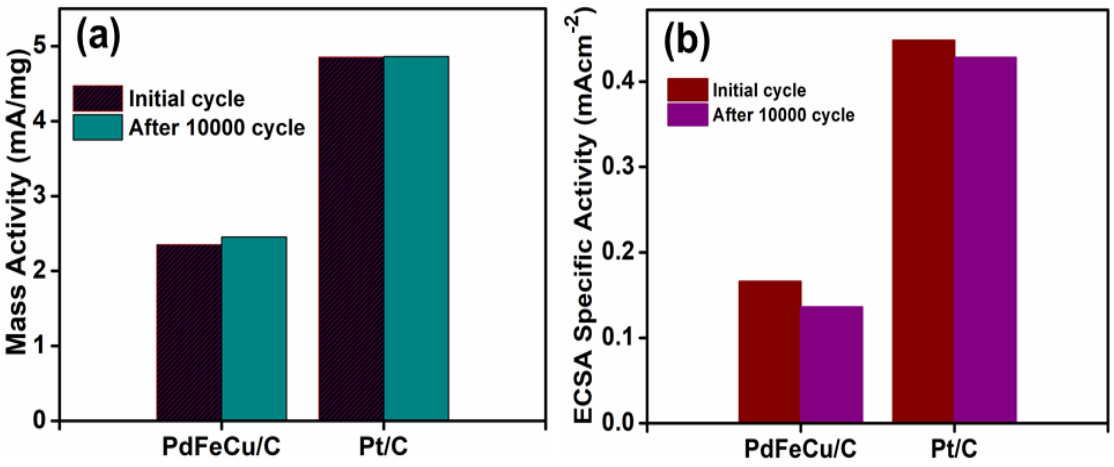

Figure 5.11: (a) Mass and (b) ECSA specific activities calculated at 0.90 V and 0.85 V *vs.* RHE of PdFeCu/C and Pt/C, respectively recorded before and after 10,000 cycles of ADT.

Table 5.4: Comparison of the ORR parameters of Pd-based electrocatalysts in 0.1 M KOH

Electrocatalyst	**E_{onset} V (*vs.* RHE)**	**$E_{1/2}$ V (*vs.* RHE)**	**Tafel slope (mV dec^{-1})**	**ECSA (m^2g^{-1})**	**References**
PdFeCu/C	0.97	0.87	52.5	91.9	This work
PdCu	1.00	0.94	60	46.82	40
PdNiRu	1.016	0.898	61.6	62.2	41
Dealloyed-CoAuPd	1.06	0.968	_	22.14	42
PdAuRu NSA	1.0336	0.893	55.31	46.08	43
Pd_3Cu_1/10N-rGO-800	_	0.80	_	38.65	44
N-rGO-Pd	0.91	0.76	_	85.34	45
Pd_2Sn nanosheets	0.973	0.893	_	33.3	46
10% Pd/MnO_2	0.866	0.780	84.7		47
PdAu-500 °C	0.982	0.827	58.6	34.968	48
Pd_3Pb	_	0.93	_	87.35	49
Pd_2CoAg	0.95	0.87	66	_	50
PdNi/C	_	0.87	_	37	51
Pd_4Au HCs/C		0.87	65		52

The ORR performance parameters of PdFeCu/C are compared to those of recently reported Pd-based electrocatalyst and presented in Table 5.4. From the comparison table it is observed that our prepared electrocatalyst has higher ECSA and lower Tafel slope values than most of the reported catalyst (e.g., PdCu [40], PdNiRu [41], dealloyed-

CoAuPd [42], PdAuRu NSA [43], Pd_3Cu_1/10N-rGO-800 [44], N-rGO-Pd [45], Pd_2Sn nanosheets [46], 10% Pd/MnO_2 [47], PdAu-500°C, [48] Pd_3Pb [49], Pd_2CoAg [50], PdNi/C [51], Pd_4Au HCs/C [52]) whereas the E_{onset} and $E_{1/2}$ values are higher and comparable. These parameters facilitate its remarkable electrochemical activity towards the ORR and the state-of-the-art improvement in the field.

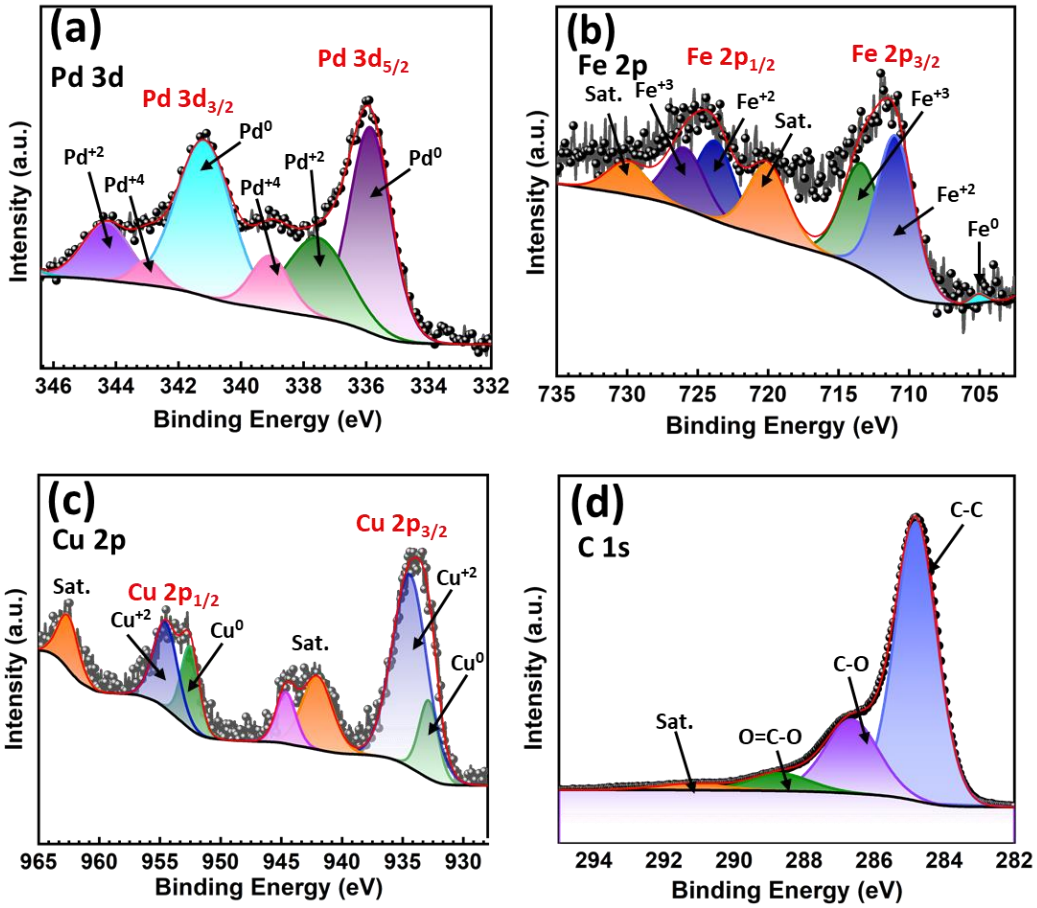

Figure 5.12: High resolution XPS spectra of (a) Pd 3d, (b) Fe 2p, (c) Cu 2p, and (d) C 1s of PdFeCu/C after 10000 ADT.

To get a direct insight into the morphology and structural properties of PdFeCu/C after the durability analysis, the XPS and TEM analysis were performed to identify their changes in morphology, composition and chemical state. After ADT analysis, the NPs were collected from the GCE surface for XPS and TEM analysis. XPS spectra indicate slight changes in the binding energy of Pd 3d, Cu 2p, Fe 2p and C 1s in PdFeCu/C were observed (Figure 5.12). Some elements spectra remain the same as a fresh catalyst; however, some additional bonding states are observed in Pd and C. Along with Pd(0) and Pd(II), Pd(IV) [53] also observed indicate significant oxidation of Pd during ADT.

Similarly, in C 1s, a satellite peak was observed. These XPS findings show that Pd, Fe, and Cu sites participated in the catalytic processes, which can improve the catalytic activities and positively influence the synergistic effect. Notably, subtle changes were detected in the morphological and structural changes, which manifest the robustness of our developed catalysts (Figure 5.13).

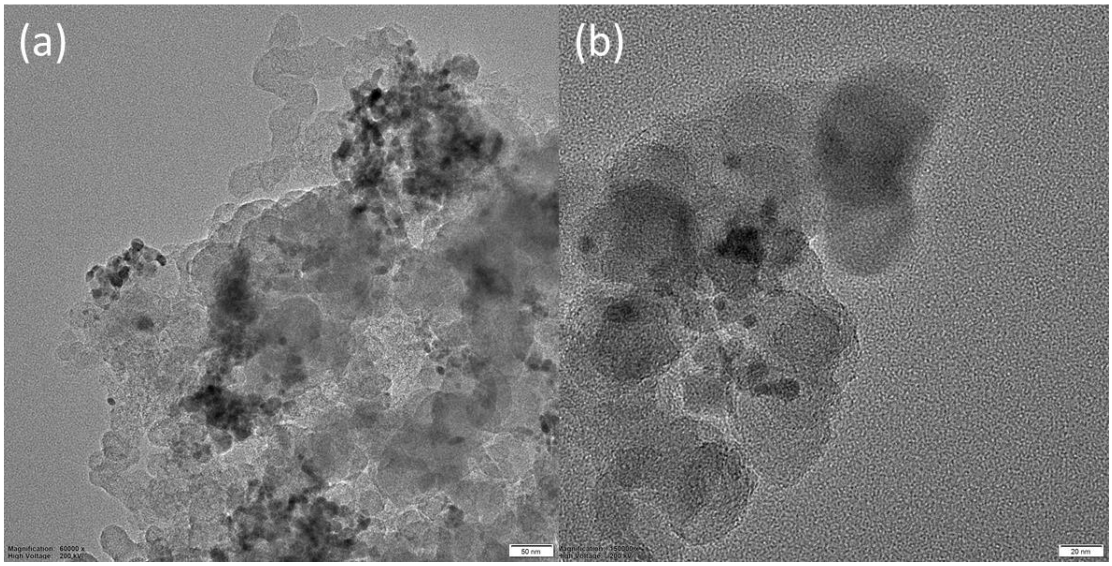

Figure 5.13: TEM image of the PdFeCu/C after 10000 ADT.

The excellent electrocatalytic performance of the as-synthesized PdFeCu/C is ascribed to the uniform embedment of PdFeCu on the carbon surface, which can inhibit the dissolution, agglomeration and Oswald ripening of the catalysts [54, 55]. The embedded PdFeCu on the carbon matrix fosters SMSI. The SMSI modifies the electronic structure of the PdFeCu/C to facilitate electron transfer between the NPs and the support, enhancing the overall electrocatalytic activity [54, 55]. The incorporation of Fe and Cu elements can greatly modify Pd's *d*-band center and electronic structure. As a result of the downshift of the *d*-band center, the interaction between the oxygen intermediate and Pd would be weakened, optimizing the adsorption energy on the catalyst's surface. That would increase the catalytic activity substantially. These results suggest that PdFeCu/C could be utilized as a high performance, low-cost and non-Pt ORR electrocatalyst.

Furthermore, it was noted that the present study has higher ORR activity, exhibiting the highest E_{onset} and $E_{1/2}$ potential, in comparison to the previous chapters (Chapters 3 and 4). The PdFeCu/C electrocatalyst exhibits remarkable performance with a Pd loading that is 17% and 42% lower in a total 20% metallic part compared to chapter 3

and chapter 4, respectively. This work may open up a new direction for those studies to resolve the present financial obstacles and develop low-loading Pd-based nanomaterials in the future.

5.3. Conclusions

In conclusion, a PdFeCu/C catalyst for ORR was designed using a simple solvothermal approach and was assessed using various physicochemical methods. The PdFeCu/C displays better ORR performance in 0.1 M KOH solution than its bimetallic counterparts and is comparable to the commercial Pt/C. Incorporating Fe and Cu in Pd lattice dramatically enhances the number of electrochemically active sites, leading to the early onset and half-wave potentials and the increased current density discussed in the preceding chapter. The downshift of the Pd *d*-band centre and Pd lattice contraction resulting from the smaller Cu and Fe atomic sizes can be related to the increase in ORR activity. As a result, our work offers new prospects for developing low-loading Pd-based nanomaterials for energy conversion devices and providing a synthetic, cost-effective method of producing electrocatalysts for ORR.

References

[1] Mukherjee, P., Kakade, B., Swami, A. current trends in platinum-based ternary alloys as promising electrocatalysts for the oxygen reduction reaction: A mini review. *Energy & Fuels*, 36(5):2306-2322, 2022.

[2] Hu, X., Yang, B., Ke, S., Liu, Y., Fang, M., Huang, Z., Min, X. Review and perspectives of carbon-supported platinum-based catalysts for proton exchange membrane fuel cells. *Energy & Fuels***,** *37*(16):11532-11566, 2023.

[3] Patowary, S., Chetry, R., Goswami, C., Chutia, B., Bharali, P. Oxygen reduction reaction catalysed by supported nanoparticles: Advancements and challenges. *ChemCatChem*, 14(7):e202101472, 2022.

[4] Mahata, A., Nair, A.S., Pathak, B. Recent advancements in Pt-nanostructure-based electrocatalysts for the oxygen reduction reaction. *Catalysis Science & Technology*, 9(18):4835-4863, 2019.

[5] Bhatt, M.D., Lee, J.Y. Advancement of platinum (Pt)-free (non-Pt precious metals) and/or metal-free (non-precious-metals) electrocatalysts in energy applications: A review and perspectives. *Energy & Fuels*, 34(6):6634-6695, 2020.

[6] Sanij, F.D., Balakrishnan, P., Leung, P., Shah, A., Su, H., Xu, Q. Advanced Pd-based nanomaterials for electro-catalytic oxygen reduction in fuel cells: A review. *International Journal of Hydrogen Energy*, 46(27):14596-14627, 2021.

[7] Zhou, M., Guo, J., Fang, J. Nanoscale design of Pd-based electrocatalysts for oxygen reduction reaction enhancement in alkaline media. *Small Structures*, 3(2):2100188, 2022.

[8] Liu, Z., Xue, J., Li, Y. Ultrathin PdCu nanosheet as bifunctional electrocatalysts for formate oxidation reaction and oxygen reduction reaction. *Small Methods*, 7(7):2300021, 2023.

[9] Wang, T., Chutia, A., Brett, D.J., Shearing, P.R., He, G., Chai, G., Parkin, I.P. Palladium alloys used as electrocatalysts for the oxygen reduction reaction. *Energy & Environmental Science*, 14(5):2639-2669, 2021.

[10] Zhang, L., Zhao, Z., Fu, X., Zhu, S., Min, Y., Xu, Q., Li, Q. Curved porous PdCu metallene as a high-efficiency bifunctional electrocatalyst for oxygen reduction and formic acid oxidation. *ACS Applied Materials & Interfaces*, 15(4):5198-5208, 2023.

[11] Hu, Y., Lu, Y., Zhao, X., Shen, T., Zhao, T., Gong, M., Chen, K., Lai, C., Zhang, J., Xin, H.L., Wang, D. Highly active N-doped carbon encapsulated Pd-Fe intermetallic nanoparticles for the oxygen reduction reaction. *Nano Research*, 13: 2365-2370, 2020.

[12] Wan, K., Chu, T., Li, B., Ming, P., Zhang, C. Rational design of atomically dispersed metal site electrocatalysts for oxygen reduction reaction. *Advanced Science*, 10(11):2203391, 2023.

[13] Zhang, J., Yang, H.B., Zhou, D., Liu, B. Adsorption energy in oxygen electrocatalysis. *Chemical Reviews*, 122(23):17028-17072, 2022.

[14] Xia, Z., Guo, S. Strain engineering of metal-based nanomaterials for energy electrocatalysis. *Chemical Society Reviews*, 48(12):3265-3278, 2019.

[15] Kluge, R.M., Haid, R.W., Riss, A., Bao, Y., Seufert, K., Schmidt, T.O., Watzele, S.A., Barth, J.V., Allegretti, F., Auwärter, W., Calle-Vallejo, F. A trade-off between ligand and strain effects optimizes the oxygen reduction activity of Pt Alloys. *Energy & Environmental Science*, 15(12):5181-5191, 2022.

[16] Goswami, C., Saikia, H., Tada, K., Tanaka, S., Sudarsanam, P., Bhargava, S.K., Bharali, P. Bimetallic palladium–nickel nanoparticles anchored on carbon as high-

performance electrocatalysts for oxygen reduction and formic acid oxidation reactions. *ACS Applied Energy Materials*, 3(9):9285-9295, 2020.

[17] Yu, D., Dong, S., Liu, Q., Jia, W., Gao, F., Wang, Y. PdM (M= Fe, Co, Ni) Bimetallic nanowires enhances oxygen reduction catalysis in acid medium. *Ionics*, 29:4825–4833, 2023.

[18] Lu, J., Luo, L., Yin, S., Hasan, S.W., Tsiakaras, P. Oxygen reduction reaction over PtFeM (M= Mo, V, W) alloy electrocatalysts: role of the compressive strain effect on Pt. *ACS Sustainable Chemistry & Engineering*, 7(19):16209-16214, 2019.

[19] Li, Z., Li, J., Jiang, K., Yuan, S., Yu, D., Wei, H., Shi, Z., Li, X., Chu, H. PdCoNi alloy nanoparticles decorated nitrogen-doped carbon nanotubes for highly active and durable oxygen reduction electrocatalysis. *Chemical Engineering Journal*, 411:128527, 2021.

[20] Li, X., Li, X., Liu, C., Huang, H., Gao, P., Ahmad, F., Luo, L., Ye, Y., Geng, Z., Wang, G., Si, R. Atomic-level construction of tensile-strained PdFe alloy surface toward highly efficient oxygen reduction electrocatalysis. *Nano Letters*, 20(2):1403-1409, 2020.

[21] Lu, Y., Jiang, Y., Gao, X., Wang, X., Chen, W. Strongly coupled Pd nanotetrahedron/tungsten oxide nanosheet hybrids with enhanced catalytic activity and stability as oxygen reduction electrocatalysts. *Journal of the American Chemical Society*, 136:11687−11697, 2014.

[22] Liang, J., Li, S., Chen, Y., Liu, X., Wang, T., Han, J., Jiao, S., Cao, R., Li, Q. Ultrathin and defect-rich intermetallic Pd_2Sn nanosheets for efficient oxygen reduction electrocatalysis. *Journal of Materials Chemistry A*, 8(31):15665-15669, 2020.

[23] Liu, S., Xiao, W., Wang, J., Zhu, J., Wu, Z., Xin, H., Wang, D. Ultralow content of Pt on Pd–Co–Cu/C ternary nanoparticles with excellent electrocatalytic activity and durability for the oxygen reduction reaction. *Nano Energy*, 27:475-481, 2016.

[24] Lüsi, M., Erikson, H., Piirsoo, H.M., Paiste, P., Aruväli, J., Kikas, A., Kisand, V., Tamm, A., Tammeveski, K. Oxygen reduction reaction on PdM/C (M= Pb, Sn, Bi) alloy nanocatalysts. *Journal of Electroanalytical Chemistry*, 917:116391, 2022.

[25] Nie, M., Xu, Z., Luo, L., Wang, Y., Gan, W., Yuan, Q. One-pot synthesis of ultrafine trimetallic PtPdCu alloy nanoparticles decorated on carbon nanotubes for

bifunctional catalysis of ethanol oxidation and oxygen reduction. *Journal of Colloid and Interface Science*, 643:26-37, 2023.

[26] Gao, F., Li, C., Ren, Y., Li, B., Lv, C., Yang, X., Zhang, X., Lu, Z., Yu, X., Li, L. High-efficient ultrathin PdCuMo porous nanosheets with abundant defects for oxygen reduction reaction. *Chemistry: A European Journal*, 28(61):e202201860, 2022.

[27] Wang, H., Ren, H., Liu, S., Yin, S., Jiao, S., Xu, Y., Li, X., Wang, Z., Wang, L. Three-dimensional PdAuRu nanospines assemblies for oxygen reduction electrocatalysis. *Chemical Engineering Journal*, 438:135539, 2022.

[28] Chetry, R., Chutia, B., Patowary, S., Borah, B.J., Sudarsanam, P., Bharali, P. Electronic modulation of Pd/C by simultaneous doping of Cu and Co tendering a highly durable and methanol-tolerant oxygen reduction electrocatalyst. *Energy & Fuels*, 37(13):9557–9567, 2023.

[29] Kawashima, K., Márquez, R.A., Son, Y.J., Guo, C., Vaidyula, R.R., Smith, L.A., Chukwuneke, C.E., Mullins, C.B. Accurate potentials of Hg/HgO electrodes: practical parameters for reporting alkaline water electrolysis overpotentials. *ACS Catalysis*, 13(3):1893-1898, 2023.

[30] Yi, S.Y., Choi, E., Jang, H.Y., Lee, S., Park, J., Choi, D., Jang, Y., Kang, H., Back, S., Jang, S. and Lee, J. Insight into defect engineering of atomically dispersed iron electrocatalysts for high-performance proton exchange membrane fuel cell. *Advanced Materials*, 35(46):2302666, 2023.

[31] Luo, L., Fu, C., Guo, Y., Cai, X., Luo, X., Tan, Z., Xue, R., Cheng, X., Shen, S., Zhang, J. Ultrafine core@shellCu_1Au_1@Cu_1Pd_3 Nanodots synergized with 3D Porous N-Doped graphene nanosheets as a high-performance multifunctional electrocatalyst. *ACS Nano*, 17(3):2992-3006, 2023.

[32] Lu, H., Kong, Z., Yang, Y., Xie, Z., Xiang, H., Liu, S., Yu, G. Highly stable PtPdCu alloy nanowire networks as oxygen reduction electrocatalysts. *Electrocatalysis*, 12:372-380, 2021.

[33] Kumar, A., Purkayastha, S.K., Guha, A.K., Das, M.R., Deka, S. Robust and promising hydrogen and oxygen evolution reactions by a nanostructured bifunctional FeCoPd alloy electrocatalyst. *Journal of Materials Chemistry A*, 10(44):23731-23743, 2022.

[34] Li, P., Xuan, Y., Jiang, B., Zhang, S., Xia, C. Hollow $La_{0.6}Sr_{0.4}Ni_{0.2}Fe_{0.75}Mo_{0.05}O_{3-\delta}$ electrodes with exsolved $FeNi_3$ in quasi-symmetrical solid oxide electrolysis cells for direct CO_2 electrolysis. *Electrochemistry Communications*, 134:107188, 2022.

[35] Liu, H., Jiang, L., Wang, Y., Wang, X., Khan, J., Zhu, Y., Xiao, J., Li, L., Han, L. Boosting oxygen reduction with coexistence of single-atomic Fe and Cu sites decorated nitrogen-doped porous carbon. *Chemical Engineering Journal*, 452:138938, 2023.

[36] Gao, Z., Chen, Z., Zhan, X., Zhou, L., Xie, Y., Yang, X., Tian, J., Zhang, G., Sun, S., Tong, X. Pt nanoparticles supported on iron and nitrogen-doped holey graphene for boosting ORR performance. *ACS Applied Nano Materials*, 6(12):10521–10530, 2023.

[37] Wang, Z., Jin, X., Chen, F., Bian, S., Li, J., Chen, J. Construction of Pt/Powder charcoal electrocatalyst utilizing MnO_2 as an additive to improve the stability for oxygen reduction reaction. *ACS Applied Engineering Materials*, 1(3):1024-1033, 2023.

[38] Wang, H., Ren, H., Liu, S., Yin, S., Jiao, S., Xu, Y., Li, X., Wang, Z., Wang, L. Three-dimensional PdAuRu nanospines assemblies for oxygen reduction electrocatalysis. *Chemical Engineering Journal*, 438:135539, 2022.

[39] Bhange, S.N., Soni, R., Singla, G., Ajithkumar, T.G., Kurungot, S. FeN_x/FeS_x-anchored carbon sheet–carbon nanotube composite electrocatalysts for oxygen reduction. *ACS Applied Nano Materials Journal*, 3(3):2234-2245, 2020.

[40] Huang, S., Wang, J., Hu, H., Li, Y., Xu, F., Duan, F., Zhu, H., Lu, S., Du, M., Bimetallic palladium-copper nanoplates with optimized d-band center simultaneously boost oxygen reduction activity and methanol tolerance. *Journal of Colloid and Interface Science*, 630:375-384, 2023.

[41] Li, X., Lu, T., Pang, H., Zhang, M., Xu, D., Xu, L., Han, M., Yang, J. Ultrathin curved PdNiRu nanosheets as bifunctional catalysts for oxygen reduction and ethylene glycol oxidation. *Nano Research*, 17(5):3777–3784, 2024.

[42] Luo, L.M., Zhang, R.H., Chen, D., Hu, Q.Y., Zhou, X.W. Synthesis of 3D thornbush-like trimetallic CoAuPd nanocatalysts and electrochemical dealloying for methanol oxidation and oxygen reduction reaction. *ACS Applied Energy Materials*, 1(6):2619-2629, 2018.

[43] Wang, H., Ren, H., Liu, S., Yin, S., Jiao, S., Xu, Y., Li, X., Wang, Z., Wang, L. Three-dimensional PdAuRu nanospines assemblies for oxygen reduction electrocatalysis. *Chemical Engineering Journal*, 438:135539, 2022.

[44] Chen, H., Bao, L., Ou, C., Wang, H., Liao, Y., Li, R., Liu, H. Highly dispersed and small-size Pd–Cu nanoparticles supported on N-doped graphene for oxygen reduction reaction catalysts. *Energy & Fuels*, 36(14):7699-7709, 2022.

[45] Ejaz, A., Jeon, S. The individual role of pyrrolic, pyridinic and graphitic nitrogen in the growth kinetics of Pd NPs on N-rGO followed by a comprehensive study on ORR. *International Journal of Hydrogen Energy*, 43(11):5690-5702, 2018.

[46] Liang, J., Li, S., Chen, Y., Liu, X., Wang, T., Han, J., Jiao, S., Cao, R., Li, Q. Ultrathin and defect-rich intermetallic Pd_2Sn nanosheets for efficient oxygen reduction electrocatalysis. *Journal of Materials Chemistry A*, 8(31):15665-15669, 2020.

[47] Cruz-Reyes, I., Trujillo-Navarrete, B., García-Tapia, K., Salazar-Gastélum, M.I., Paraguay-Delgado, F., Félix-Navarro, R.M. Pd/MnO_2 as a bifunctional electrocatalyst for potential application in alkaline fuel cells. *Fuel*, 279:118470, 2020.

[48] Hu, Q., Zhan, W., Guo, Y., Luo, L., Zhang, R., Chen, D., Zhou, X. Heat treatment bimetallic PdAu nanocatalyst for oxygen reduction reaction. *Journal of Energy Chemistry*, 40:217-223, 2020.

[49] Fu, L., Liu, K., Lyu, Z., Sun, Y., Cai, J., Wang, S., Wang, Q., Xie, S. Two-dimensional template-directed synthesis of one-dimensional kink-rich Pd_3Pb nanowires for efficient oxygen reduction. *Journal of Colloid and Interface Science*, 634:827-835, 2023.

[50] Liu, S., Zhang, H., Mu, X., Chen, C. Surface reconstruction engineering of twinned Pd_2CoAg nanocrystals by atomic vacancy inducement for hydrogen evolution and oxygen reduction reactions. *Applied Catalysis B: Environment and Energy*, 241:424-429, 2019.

[51] Lu, X., Ahmadi, M., DiSalvo, F.J., Abruña, H.D. Enhancing the electrocatalytic activity of Pd/M (M= Ni, Mn) nanoparticles for the oxygen reduction reaction in alkaline media through electrochemical dealloying. *ACS Catalysis*, 10(10):5891-5898, 2020.

[52] Jiao, W., Chen, C., You, W., Zhao, X., Zhang, J., Feng, Y., Wang, P., Che, R. Hollow Nanochains: Hollow palladium-gold nanochains with periodic concave structures as superior ORR electrocatalysts and highly efficient SERS substrates. *Advanced Energy Materials*, 10(18):2070082, 2020.

[53] Lisowski, W., Keim, E.G. Vacuum annealing phenomena in ultrathin TiD_y/Pd bi-layer films evaporated on Si(100) as studied by TEM and XPS. *Analytical and Bioanalytical Chemistry*, 396:2797-2804, 2010.

[54] Luo, Z., Zhao, G., Pan, H., Sun, W. Strong metal–support interaction in heterogeneous catalysts. *Advanced Energy Materials*, 12(37):2201395, 2022.

[55] Yan, Q.Q., Yin, P., Liang, H.W. Engineering the electronic interaction between metals and carbon supports for oxygen/hydrogen electrocatalysis. *ACS Materials Letters*, 3(8):1197-1212, 2021.